Investigation of Viscor and Methanol Spray Dynamics using Proper Orthogonal Decomposition in Siemens Energy Industrial Atomisers

Ali Alshahrani[1], Izwan Mohni, Adesile Ajisafe, Midhat Talibi, Ramanarayanan Balachandran, Andrea Ducci[1]
Department of Mechanical Engineering,
University College London,
Torrington Place,
London WC1E 7JE, United Kingdom
email: ali.alshahrani.21@ucl.ac.uk,
a.ducci@ucl.ac.uk

Marc Furi, Michel Houde
Siemens Energy Canada Ltd SE GS PRM
NT FFH 9505,
Cote de Liesse Road,
Montreal QC H9P 1A5, Canada

Suresh Sadasivuni, Geoff Engelbrecht, Ghenadie Bulat
Siemens Energy Industrial Turbomachinery Ltd,
PO Box-1, Waterside South,
Lincoln, LN57FD, United Kingdom

The demand to reduce carbon emissions has prompted research into alternative fuels that can replace conventional fuels like diesel in industrial gas turbines. Among different potential biofuels and e-fuels, methanol emerges as a sustainable and high-performance alternative to diesel for gas turbine applications. It is well established that the fuel physical properties, spray dynamics and degree of atomisation are strongly correlated and affect the engine performance. In this study, Proper Orthogonal Decomposition (POD) was applied on spatio-temporally resolved images to characterise Viscor, here used as diesel surrogate, and methanol sprays of pressure-swirl atomisers employed in Siemens Energy industrial gas turbine (SGT-400) combustors. The methanol experimental results were then compared against Viscor results at analogous operating conditions, including density adjusted atomiser pressure drop and ambient pressures. Results confirmed that methanol spray cone angle is slightly wider than Viscor at corresponding operating conditions. The POD analysis allowed to identify dominant spatial oscillation modes and characterise them in terms of oscillation amplitude, wavelength and onset distance from the atomiser edge for both fuels. Oscillations wavelengths and maximum amplitudes were found to correlate with Weber number, average SMD and axial jet velocities.

Keywords: Atomisation, methanol, spray dynamics, POD, alternative fuels

1 Introduction

Increasingly strict regulations on emissions from the power sector have spurred on the search for alternative fuels such as methanol as direct substitutes for conventional fossil fuels like diesel. Methanol, despite being classed as a hydrocarbon fuel, has shown promising results with lower CO_2 emissions, as well as lower NO_X emissions (up to 75% and 45% lower compared to distillate and natural gas, respectively) due to its lower flame temperature, as compared to conventional fuels [1–3]. Furthermore, growing interests in e-fuels and increasing investment in hydrogen generation provide further opportunity for decarbonisation of gas turbine liquid fleets through e-methanol. Industry interest in energy generation through methanol is reflected in recent efforts by Siemens Energy's installation of the world's largest e-methanol production facility in Denmark [4] and their successful demonstration of an SGT-A20 gas turbine running on green methanol in Aberdeen, Scotland, where an 80% reduction in NO_X was achieved [5].

In the context of spray combustion, the spray features (which affect the quality of atomisation and hence its combustion) observed for methanol are different to that of diesel. Yanfeng *et al.* [6] demonstrated that at equal pressure drop methanol sprays are characterised by slightly shorter penetration lengths, slightly lower penetration velocities, and slightly larger spray cone angles compared to diesel likely due to its lower density and viscosity. Wang *et al.* [7] confirmed these observations and reported a smaller liquid phase area of the methanol spray, which was attributed to higher evaporation rates.

In terms of microscopic spray features, the numerical study of Wang *et al.* [8] showed that methanol, 5 ms after injection, has a slightly larger overall droplet size compared to gasoline: 15.6 μm and 17.3 μm for methanol and 14.1 μm and 15.6 μm for gasoline at back pressures 0.1 and 1 MPa, respectively. The different properties of methanol compared to conventional fuels also play a role in macroscopic spray features where, in a multi-hole injector, it was reported that methanol has a larger spray angle than that of gasoline, although the authors observed smaller Sauter mean diameters (SMD) compared to that of gasoline, contrary to the previously mentioned observations [9]. Methanol also exhibits smaller SMD values compared to diesel, as reported by Aigal *et al.* [10].

A key characteristic of sprays that plays a primary role in atomisation quality is the spray cone angle. As the spray cone angle increases, the turbulent interactions between droplets and the surrounding ambient gas increases, which in turn enhances breakup [11]. Sprays in practical applications are often unsteady due to turbulence or the existence of coherent flow structures which perturbs the spray surface. As the spray cone angle is obtained from a time-averaged image of the spray, the surface wave fluctuations are not captured. Details of spatio-temporal variation of the spray surface can provide insights into atomisation and spray formation in greater detail. A possible way of characterising the time variation of the spray surface is with the application of proper orthogonal decomposition (POD).

In engineering applications, liquid fuel sprays often exhibit dominant flow features which are sometimes hidden by small-scale turbulence, which make them difficult to observe directly. First introduced by Lumley [12], POD is a linear correlation method of data analysis that, in the field of fluid dynamics, is conventionally used to identify coherent flow structures and to recreate low order models of the flow. The principle behind POD is to extract from time-resolved data (e.g. vector/scalar fields) a set of basis functions or "modes", both temporal as well as spatial, which are ranked by

[1]Corresponding Author.

their prominence, often referred to as "energy" content. Application of POD to sprays would allow detailed characterisation of dynamic features and key mechanisms.

The implementation of POD on time-resolved images of spray and liquid jets has provided an explanation for different phenomena within these flows. Rajamanickam and Basu [13] applied POD to instantaneous particle image velocimetry (PIV) to study the interactions of a hollow-cone liquid sheet with a coannular swirling air flow. They also applied POD to high-speed shadowgraphy images and found that spray-swirl interactions are dominated by Kelvin-Helmholtz instabilities due to strong shear at the inner and outer layers of the spray.

Arienti and Soteriou [14] found that POD analysis applied to high-speed shadowgraphy images of a fuel-jet in cross flow allowed them to identify dominant frequencies of the spray, consistent with those found through a linear Kelvin-Helmholtz instability analysis. In their study, they estimated dominant wavelengths of the jet dynamics by averaging the distances between consecutive peaks and troughs of dominant POD mode. Similarly, Kang *et al.* [15] applied POD to instantaneous profiles of a spray boundary, which were identified through an edge detection method applied to shadowgraphy images. This allowed them to measure dominant wavelengths and frequencies at the jet boundaries.

By using Mie scattering images of a pressure swirl atomiser, Ajisafe *et al.* [16] used POD and dynamic mode decomposition (DMD) on Mie scattering images of a turbulent pressure swirl atomiser spray and found that the size of large coherent structures in the POD modes increased with pressure drop and ambient pressure.

In our study, we distinguish the dynamical behaviour between methanol and diesel by means of POD applied to high-speed Mie scattering images of a spray generated by a Siemens Energy pressure swirl atomiser. To the authors' knowledge, while POD is applied extensively to liquid atomisation even for combustion applications such as diesel sprays, this is the first time POD is used as a means of comparing the spray dynamics of methanol to that of diesel. Furthermore, for the first time, the outcomes from POD analysis for an industrial atomiser was directly correlated to the measured droplet distribution and velocity characteristics.

2 Methodology

2.1 Experimental Setup.

2.1.1 High-speed Mie scattering imaging. The tests were carried out in a cylindrical high-pressure vessel with an inner diameter of 300 mm and internal volume of about 23 L. The vessel is capable of withstanding ambient conditions up to 100 bar pressure and 800 K temperature and is equipped with four quartz glass windows of 120 mm in diameter to gain optical access to the spray. Compressed air of high purity (zero grade) is used to increase the ambient pressure p_a inside the vessel. Viscor calibration fluid (a surrogate for diesel) and methanol are pressurised using zero grade compressed nitrogen gas to a fuel supply pressure p_f, and injected into the vessel using a Siemens Energy simplex pressure swirl atomiser employed in SGT-400 gas turbine combustors. The system is operated through a purpose-built Labview interface to gain full control of vessel filling and emptying processes, as well as to allow synchronisation of fuel injection timing with the optical diagnostic measurement system. Full details of the experimental procedure can be found in our previous work [17].

The experimental conditions selected for the current study allow comparison of spray characteristics of Viscor and methanol for the same atomiser. The boundary conditions for Viscor are based on typical operating conditions for diesel in a small gas turbine engine. The heating value of methanol is roughly half that of diesel. To address this issue there are three possible ways: i) increasing the pressure drop and therefore the mass flow rate significantly, ii) changing the design of the nozzle, and iii) increase the number of nozzles. In order to minimally impact the spray characteristics the third option is the preferred one. In this work, the pressure drop

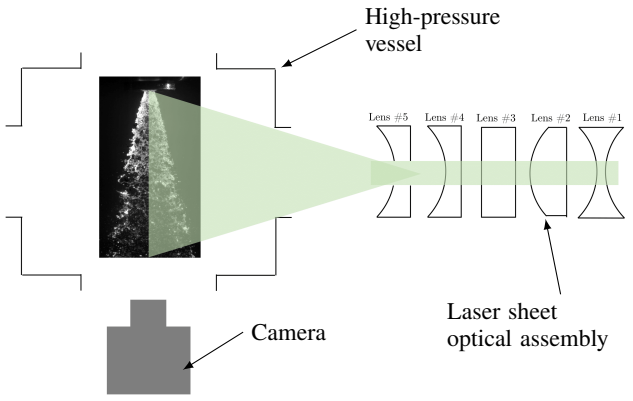

Fig. 1 SIMPLIFIED SCHEMATIC OF THE EXPERIMENTAL SETUP.

was adjusted to account for the fuels' density ratio (i.e. 1.15). The experimental matrix was developed based on this approach. Three sets of experimental conditions were investigated. The first two sets involved Viscor and methanol measurements at the same pressure difference and inlet fuel pressure conditions, while in the last set the fuel pressure of methanol was multiplied by a factor of 1.15 to account for the different density between Viscor and methanol (i.e., $p_{fm}/p_{fv} = 1.15$). Each set comprises twelve test points with different combinations of pressure drop, Δp, ambient pressure, p_a, and fuel pressure, p_f. A total of thirty-six conditions were tested and the corresponding spray cone angles were estimated. POD was applied to the eleven conditions reported in Table 1. Pressure drop $\Delta p = p_f - p_a$ is varied between 1 - 17.25 bar, with p_a = 1 - 11 bar, corresponding to aerodynamic Weber number, We = 6 - 1050 and Reynolds number, Re = 4000 - 55000, defined in Eqs. 1 and 2

$$We = \rho_a U_b^2 d_o/\sigma_l \tag{1}$$

$$Re = \rho_l U_b d_o/\mu_l \tag{2}$$

where ρ_a and ρ_l are the ambient and liquid density, respectively, $U_b = \sqrt{2\Delta p/\rho_l}$ is the liquid bulk velocity, d_o is the nozzle orifice diameter, σ_l is the liquid surface tension, and μ_l is the liquid dynamic viscosity.

A schematic of the set-up for the Mie scattering spray measurement is shown in Fig. 1. A laser sheet with a thickness of ≈ 0.4 mm bisected and illuminated the spray cross-section, and the Mie-scattered light was imaged with a Phantom VEO 710 camera (frame rate of 6.7 & 7.5 kHz at 1280 x 800 pixel resolution) equipped with a 100 mm lens set at an aperture of f/11, resulting in a measurement area of 41.4 × 27.5 mm. The laser sheet was created using a custom compound lens system that included a set of one Thorlabs LD-1464A (Lens #1) spherical concave lens (focal length of -50 ± 0.50 mm), one Thorlabs LJ1695RM (Lens #2) cylindrical convex lens (focal length of 50 ± 0.50 mm), one Thorlabs LJ1703RM (Lens #3) cylindrical convex lens (focal length of 75 ± 0.75 mm), and two Thorlabs LK1336RM (Lenses #4 and #5) cylindrical concave lenses (focal length of -50 ± 0.50 mm) placed in front of a Nd:YLF high-speed laser (Litron LDY304-PIV). The laser and camera were controlled through TSI Insight 4G and Phantom Camera software and synchronised through Labview to the fuel injection valve signal. TSI LaserPulse Synchronizer Model 610036 is used to synchronise the signals between the camera trigger, injection trigger, and laser. Only images acquired during the spray steady state (532 images ≈ 0.08 and 0.07 s for 6.7 & 7.5 kHz frame rate, respectively) were post-processed to measure cone angles and assess the spray dynamics with POD.

Table 1 POD Test Matrix.

Fuel	Δp (bar)	p_f (bar)	p_a (bar)	We (-)	$10^3/\ Re$ (-)
Viscor	1	2	1	6	4
Methanol	1	2	1	8	14
Viscor	3	4	1	19	7
Methanol	3	4	1	25	24
Viscor	3	14	11	203	7
Methanol	3	14	11	263	24
Viscor	15	16	1	97	15
Methanol	15	16	1	125	55
Adj-Methanol	17.25	18.25	1	144	59
Viscor	15	26	11	1015	15
Methanol	15	26	11	1316	55

2.1.2 Phase Doppler Particle Analyser (PDPA) System. Besides high-speed imaging, Phase Doppler Particle Analyser (PDPA) measurements were also carried out to obtain point estimates of droplet size and velocity of the Viscor spray. The TSI-PDPA system consists of two pairs of laser beams, wavelengths 514.5 and 488 nm, generated by a TSI beam-splitter unit placed in front of a water-cooled Argon-Ion laser. Fibre optics take the pairs of laser beams to the emitting probe (Model TM250), which converge them down through a 500 mm focal length lens (Model TLN05-500). As a result, the dimensions of the control volume are 0.184×0.184×4.9 mm^3 and 0.175×0.175×4.6 mm^3 for the green and blue channels, respectively. The scattered-light collector unit (Model RV2070-500 with a 500mm focal length lens, TLN07-500) placed on the opposite side of the laser emitting probe at an angle of 15° with respect to the probe axis. Radial profiles of droplet size as well as axial and radial velocity components were obtained at an axial distance of 16 mm downstream of the nozzle with a radial resolution of 0.5 mm. PDPA measurements were conducted in the radial direction on both sides of the spray until the droplet data rate exhibited a sharp decrease (for reference, the maximum data rate was approximately 50 kHz). An Intensity Validation method, which is based on a Gaussian distribution of the signal burst obtained when a droplet crosses the control volume, was also applied to further increase the accuracy of the measured droplets (40% increase in accuracy) [18]. As a consequence, the PDPA measurement uncertainties were estimated to be ≈3% and ≈7% for droplet velocity and diameter, respectively.

2.2 Spray Boundary Detection. Firstly, the instantaneous images are enhanced using contrast-limited adaptive histograph equalization (CLAHE) [19] and Gaussian-filtered with a standard deviation of 2. The average spray image is then obtained. A multilevel thresholding algorithm based on Otsu's method [20] is then applied to obtain the segmented mean spray image, on which Sobel edge detection is used to extract the mean spray boundary. Smoothing is then applied to the boundary, which then is used to calculate the spray cone angle θ. The calculated mean spray boundary is shown in Fig. 2, where $\theta = \theta_1 + \theta_2$. Applying a similar protocol to the instantaneous images, the instantaneous surface waves of the spray are obtained by selecting the region around the right side of the spray, shown in Fig. 3(a). The centre line of the region is aligned with the mean spray boundary, and its width is adjusted to fully capture the spray surface. The selected region is then rotated by 90-θ_1/2 and cropped from the instantaneous images. The Sobel method is then applied to detect the surface wave, as demonstrated in Fig. 3(b). The selected region is limited to ≈ 20 mm downstream from the nozzle tip as the algorithm fails to correctly identify the spray boundary beyond this point in most test conditions.

2.3 Proper Orthogonal Decomposition of Spray Boundary. The instantaneous spray boundary profiles, $I(x,t)$, identified in the previous section for each test condition were then further analysed through POD to identify coherent oscillation characteristics (i.e. wavelength and frequency) occurring at the spray edges. The instantaneous spray boundary profiles were arranged in the $\mathbf{I}(x,t)$ matrix defined in Eq. 3

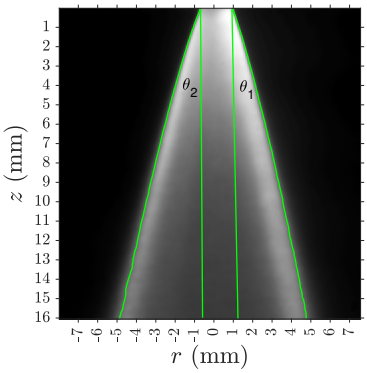

Fig. 2 MEAN SPRAY BOUNDARY.

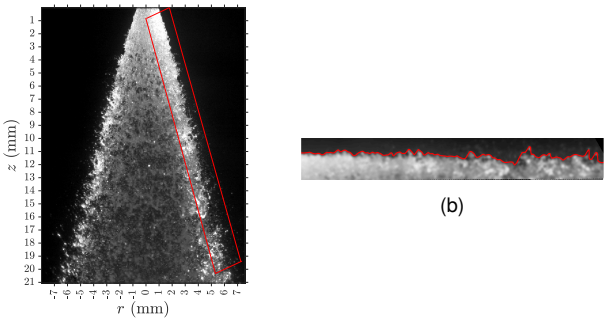

Fig. 3 a) THE SELECTED REGION FOR INSTANTANEOUS SPRAY SURFACE WAVES AND b) ROTATED SELECTED REGION WITH DETECTED SPRAY BOUNDARY.

$$\mathbf{I}(x,t) = \begin{bmatrix} I_{11} & \dots & I_{1n} \\ \vdots & \ddots & \vdots \\ I_{m1} & \dots & I_{mn} \end{bmatrix} \quad (3)$$

where m and n are the total number of instantaneous profiles and the total number of axial locations along the profile, respectively. When applying POD the covariance/correlation matrix of $\mathbf{I}$ and its eigenvalues, λ_i and eigenvectors, are estimated, and the corresponding temporal, $a_i(t)$, and spatial mode functions, $\mathbf{\Phi}_i(x)$, are found. Modes are ordered in terms of prominence, "energy" content, which is captured by the magnitude of the corresponding eigenvalue, λ_i, i.e. larger values of λ_i are associated to modes dominating the spray boundary oscillations. Reconstruction of the original instantaneous spray profiles, I, is obtained by adding each mode contribution, $a_i(t)\mathbf{\Phi}_i(x)$, according to Eq. 4.

$$I(x,t) = \sum_{i=1}^{m} a_i(t)\mathbf{\Phi}_i(x) \quad (4)$$

3 Results and Discussion

3.1 Spray Cone Angle. A comparison between methanol and Viscor spray cone angles, θ, are shown in Figs. 4(a) and 4(b) for standard and density adjusted conditions, respectively. All sets of data exhibit a similar behaviour for both fuels, with a sharp increase of cone angle at low pressure drops and a lower gradient as Δp is further increased. This behaviour is expected for pressure-swirl atomisers, where the spray cone angle widens with pressure drop

until it attains a maximum value before it starts contracting again [for example see 11, 21, 22].

When directly comparing the cone angle for the two fuels, methanol sprays are characterised by marginally wider cone angles than Viscor sprays at corresponding injection and ambient pressure conditions. This is also valid for the density-adjusted pressure drop conditions, Fig. 4(b), where cone angle differences between the two fluids are smaller ($\Delta\theta_{max} \approx 3°$), and their values get closer, i.e. within 3°, with increasing ambient pressure. Current results are in good agreement with the literature [7, 8].

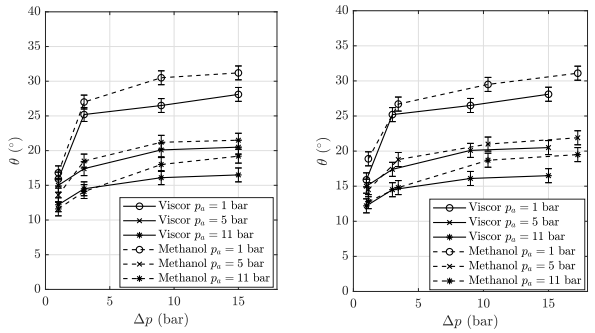

Fig. 4 SPRAY CONE ANGLE (θ) FOR VISCOR AND METHANOL FOR A) STANDARD AND B) DENSITY-ADJUSTED CONDITIONS.

3.2 Proper Orthogonal Decomposition. The cone angle only captures the time-averaged macroscopic behaviour of a spray, and from this aspect only marginal differences were found between the two fluids. In this section, POD was used to investigate the time dynamics of the two fuel sprays and to identify dominant modes of oscillations at the spray edges. Given the small differences in cone angle of Figs. 4 (a, b), POD was mainly applied to standard test conditions (see Table 1), limiting the analysis to one density-adjusted test point, Δp = 17.25 bar and p_a = 1 bar.

Figs. 5(a), 5(b) and 5(c), 5(d) show the variation of the cumulative energy distribution with increasing number of POD modes at different operating conditions, pressure drop Δp and ambient pressures p_a = 1 and 11 bar, for Viscor and methanol, respectively. When considering all data sets, it is clear that the first few modes play a prominent role in the spray dynamics, as a very sharp increase in $\sum \lambda$ is seen at the lower end of mode numbers. For example, nearly 17% of the total "energy" content is present in the first three modes for Viscor and methanol conditions at p_a = 1 bar and lower values of Δp = 1 and 3 bar. The number of modes accounting for 17% of the total "energy" content tend to increase to a maximum of 5 when larger pressure differences and ambient pressure are considered, Δp = 15 bar and p_a = 11 bar. It is also worth to note that the cumulative energy distributions for the standard (Δp = 15 bar) and density-adjusted methanol (Δp = 17.25 bar) conditions show little differences and are characterised by a nearly identical growth rate with mode number. In the rest of the analysis, the spatial and temporal functions of modes accounting for the first 17% of the total "energy" content are further analysed and discussed.

The variations in space of the spatial modes accounting for 17% of the "energy" content for Viscor at all the different test conditions are shown in Fig. 6. To compare on even ground the different modes and take into account the corresponding magnitude of spray boundary oscillation, the profiles shown in Fig. 6 were estimated according to Eq. 5

$$A_i(x) = \|a_{i-max}\| \mathbf{\Phi}_i(x) \tag{5}$$

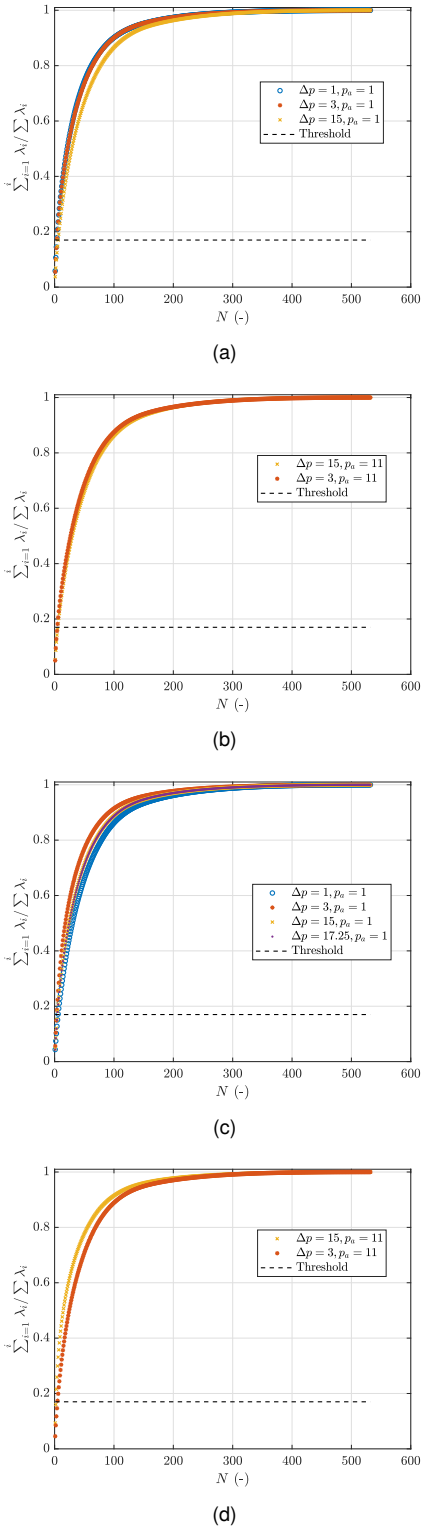

Fig. 5 POD CUMULATIVE ENERGY DISTRIBUTION WITH INCREASING MODE NUMBER FOR: A) VISCOR, p_a = 1 BAR, B) VISCOR, p_a = 11 BAR c) METHANOL, p_a = 1 BAR, d) METHANOL, p_a = 11 BAR.

where $\|a_{i-max}\|$ is the maximum absolute value of the temporal coefficient in time, $a_i(t)$. From Fig. 6 it is evident that all A_i-profiles exhibit a similar behaviour with growing oscillation waves that arise at an onset distance downstream from the nozzle. As expected, lower modes are associated with larger scale structures with higher oscillation magnitude and longer oscillation wavelength. When considering a constant ambient pressure, p_a = 1 bar (cf Figs. 6 a, b and c) two physical aspects in the wave behaviour can be seen: 1) wave oscillations are larger (threefold) for smaller pressure differences; 2) the onset distance of oscillations moves downstream, away from the atomiser, when the pressure difference is increased. These aspects are also valid when an ambient pressure p_a = 11 bar is considered, where maximum absolute values of mode 1 oscillations are $\approx$ 1.4 mm and $\approx$ 1 mm for Δp = 3 bar and 15 bar, respectively. Similarly, the wave onset distance moves from 8 mm to 12 mm away from the nozzle as the pressure difference is increased. Finally, when comparing different ambient pressure, p_a = 1 and 11 bar, for a fixed pressure difference, Δp = 3 bar, (cf Figs. 6 b and d), the oscillation magnitude decreases by two-fold as the ambient pressure is increased, while the oscillation onset distance gets shorter.

Similar trends are also exhibited by the methanol A_i-profiles shown in Fig. 7 for all standard and density-adjusted test conditions. When comparing Viscor and methanol A_i-profiles for analogous test conditions at p_a = 1 bar (cf Figs. 6 a-c vs 7 a-c) it seems that the oscillation magnitude is little affected while the oscillation onset moves downstream when methanol is employed. For example, at Δp = 1 bar, onset distances are 8 mm for Viscor and 12 mm for methanol, while at Δp = 3 bar, they are 12 mm and 14 mm for Viscor and methanol, respectively.

A direct comparison of different characteristics extracted from mode 1 for all Viscor and methanol data sets are shown in Figs. 8 and 9, where maximum oscillation amplitudes are plotted against pressure difference, Δp, and Weber number, We, respectively, while Figs. 10 and 11, provide the variation of mode 1 wavelength, λ_{Φ_1}, and period, T_{Φ_1}, with Weber number, respectively. The wavelength was directly estimated from the distances between mode 1 crests and troughs of Figs. 6 and 7, while the period of oscillation was found by dividing the wavelength with the bulk velocity, $T_{\Phi_1} = \lambda_{\Phi_1}/U_b$. From this set of figures it is clear that the two fuels exhibit very similar dynamic behaviours, with both sets of data being denoted by a similar decrease in amplitude, wavelength and period as the pressure difference and Weber number are increased. This implies that the combustion performance is expected to be similar between the two fuels, while emission performance would be mainly determined by the combustion kinetics. This builds further confidence in methanol as a viable fuel source to reduce NO_x and carbon emissions, for a smooth transition between diesel and methanol with minimal retrofitting of current GT technology and without compromising on performance.

These phenomena can be explained by the shorter breakup length of the liquid sheet with higher pressure difference, which results in reduced boundary fluctuations and smaller droplets [23]. Similarly, in agreement with the work of Reitz and Bracco [24], higher Weber number related to higher jet velocities and aerodynamic forces promote modes with shorter wavelengths and smaller periods of spray boundary oscillations.

Besides the spatial functions of Figs. 6 and 7, also the mode temporal functions were further post-processed with an FFT analysis to identify dominant mode time-scales. Figs. 12 (a-d) show the power spectrum density (PSD) of the POD temporal coefficients of the first set of modes accounting for 17% of the total "energy" content. Each plot is normalised with the corresponding maximum value at each condition. Contrary to the spatial functions, the temporal coefficients do not display a dominant frequency of oscillations, indicating that temporal variations are more random and less structured than spatial ones. These findings are in general agreement with those of [16], who directly applied POD and DMD to Mie-scattered images with the same atomisers of the current work.

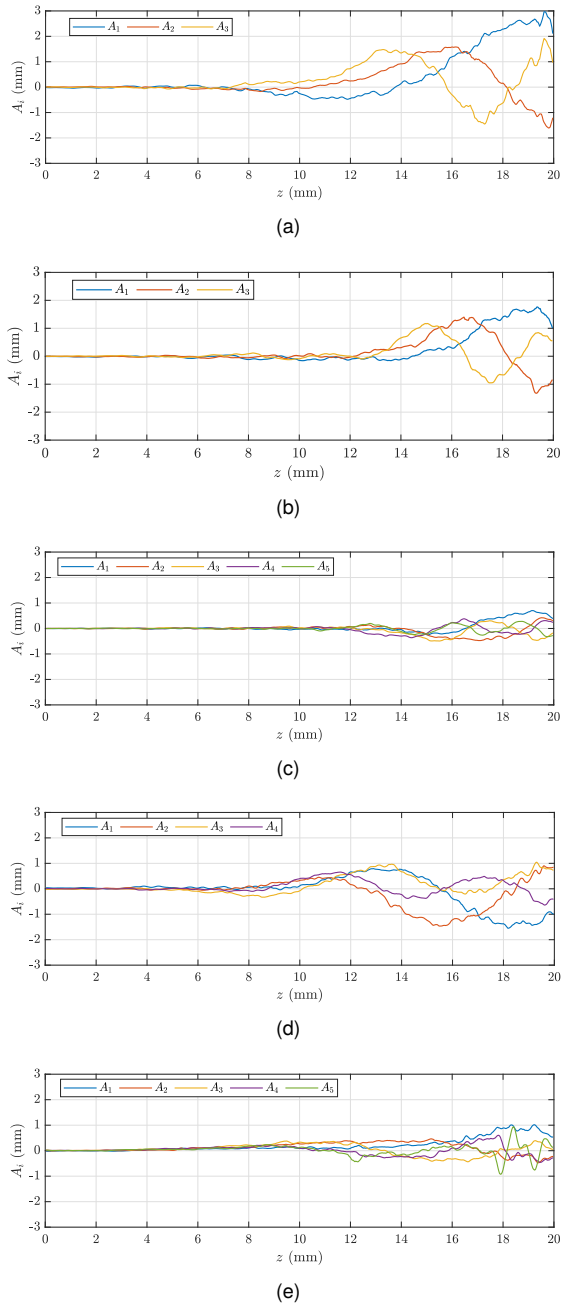

Fig. 6 SPRAY BOUNDARY OSCILLATIONS OF MODES ACCOUNTING FOR 17% OF TOTAL "ENERGY" CONTENT (VISCOR): A) Δp = 1 BAR, p_a = 1 BAR, B) Δp = 3 BAR, p_a = 1 BAR, C) Δp = 15 BAR, p_a = 1 BAR, D) Δp = 3 BAR, p_a = 11 BAR, E) Δp = 15 BAR, p_a = 11 BAR.

3.3 Droplet size and velocity. The radial profile of normalised Sauter Mean Diameter (SMD) and time-averaged droplet axial velocity, U_x, are shown in Figs. 13 (a, b) for Viscor fuel [17] and Figs. 14 (a, b) for methanol fuel at a distance of 16 mm downstream of the atomiser tip. For proprietary reasons the actual SMD values cannot be disclosed and in Figs. 13 (a) and 14 (a) it has been normalised with the spatially-averaged value, $\overline{SMD}_r$, at the reference operating condition (here, p_a = 1 bar and Δp = 1 bar). It is observed that, generally, with higher pressure drops, the droplet size decreases. As the fuel is subjected to higher velocities and more turbulence, the breakup is enhanced, resulting in smaller droplets. At higher ambient pressures, larger droplets

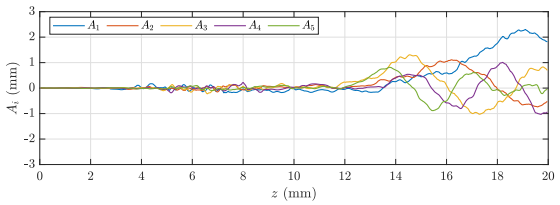

(a)

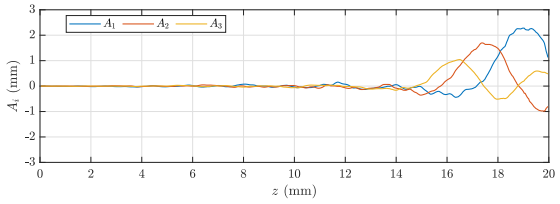

(b)

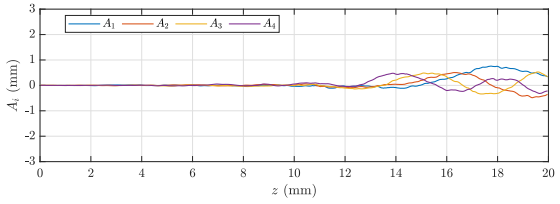

(c)

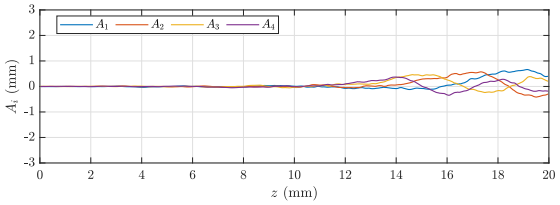

(d)

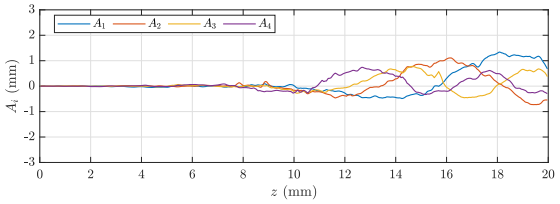

(e)

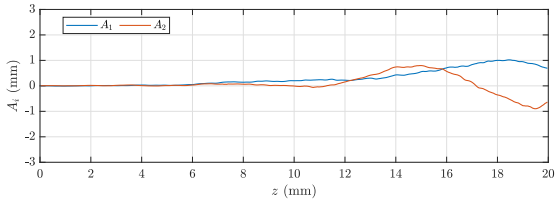

(f)

Fig. 7 SPRAY BOUNDARY OSCILLATIONS OF MODES ACCOUNTING FOR 17% OF TOTAL "ENERGY" CONTENT (METHANOL): A)Δp = 1 BAR, p_a = 1 BAR, B) Δp = 3 BAR, p_a = 1 BAR, C) Δp = 15 BAR, p_a = 1 BAR, D) Δp = 17.25 BAR, p_a = 1 BAR, E) Δp = 3 BAR, p_a = 11 BAR, f) Δp = 15 BAR, p_a = 11 BAR.

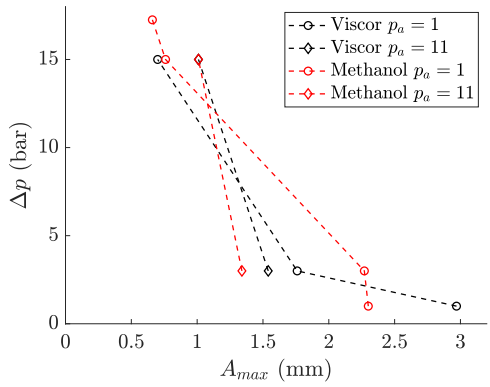

Fig. 8 VARIATION OF PRESSURE DROP WITH MAXIMUM AMPLITUDE OF SURFACE WAVES.

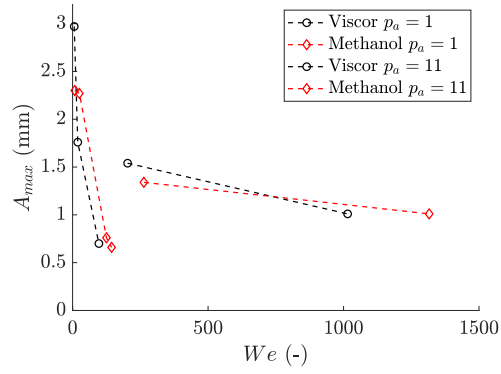

Fig. 9 VARIATION OF MAXIMUM AMPLITUDE OF SURFACE WAVES AGAINST WEBER NUMBER.

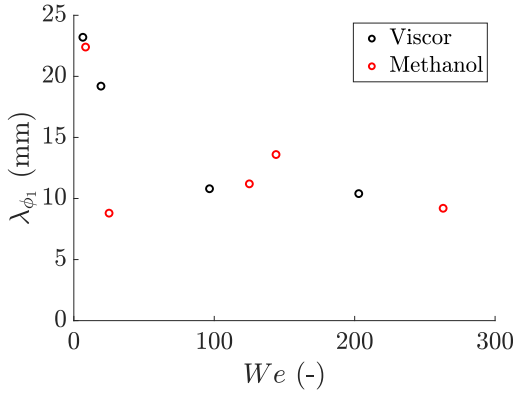

Fig. 10 WAVELENGTHS OF THE FIRST POD MODE PLOTTED AGAINST WEBER NUMBER.

are formed due to the spray contraction resulting in droplet coalescence. When comparing the two fuels, i.e. Figs 13 (a) and 14 (a), the SMD of methanol is generally smaller than that of Viscor. It is worth noting that very similar SMD_r were observed for both fuels at the reference condition, p_a = 1 bar, Δp = 1 bar). Methanol spray is also characterised by higher axial velocity, U_x, than Viscor (cf. Figs 13b and 14b). These differences might be attributed to methanol lower viscosity and lower evaporation temperature, resulting in higher atomisation and lower frictional losses.

An attempt to correlate the variation of the normalised SMD and axial velocity with the maximum oscillation amplitudes of the

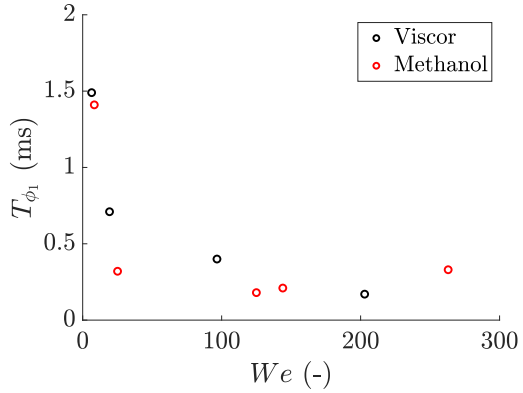

Fig. 11 PERIODS OF THE FIRST POD MODE PLOTTED AGAINST WEBER NUMBER.

spray boundary extracted from the POD analysis is provided in Figs. 15 (a) and (b), respectively.

It is evident that larger spray boundary fluctuations are related to larger droplet diameters. This behaviour is expected as larger fluctuations are also associated to longer oscillation wavelengths (cf Fig. 10) and smaller pressure drops with reduced droplet atomisation. These trends are generally valid for both fuels, except at p_a = 1 bar and Δp = 1 bar, where methanol exhibits normalised SMD values close to Viscor, but reduced amplitude of spray boundary fluctuations. This could be explained by considering that methanol is characterised by higher axial velocity (20% higher), which promotes stability and reduced boundary fluctuations for all test conditions investigated (as shown in Fig. 15).

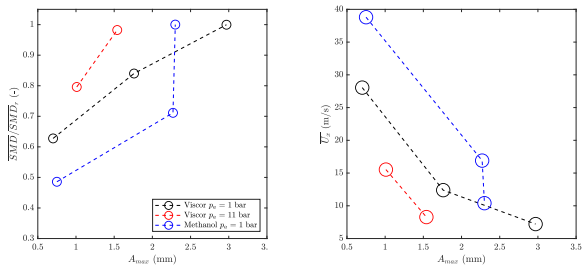

(a) (b)

Fig. 15 VARIATION OF A) NORMALISED SMD and B) U_x AGAINST A_{max} FOR BOTH VISCOR (1 AND 11 BAR) AND METHANOL (1 BAR) TEST CONDITIONS.

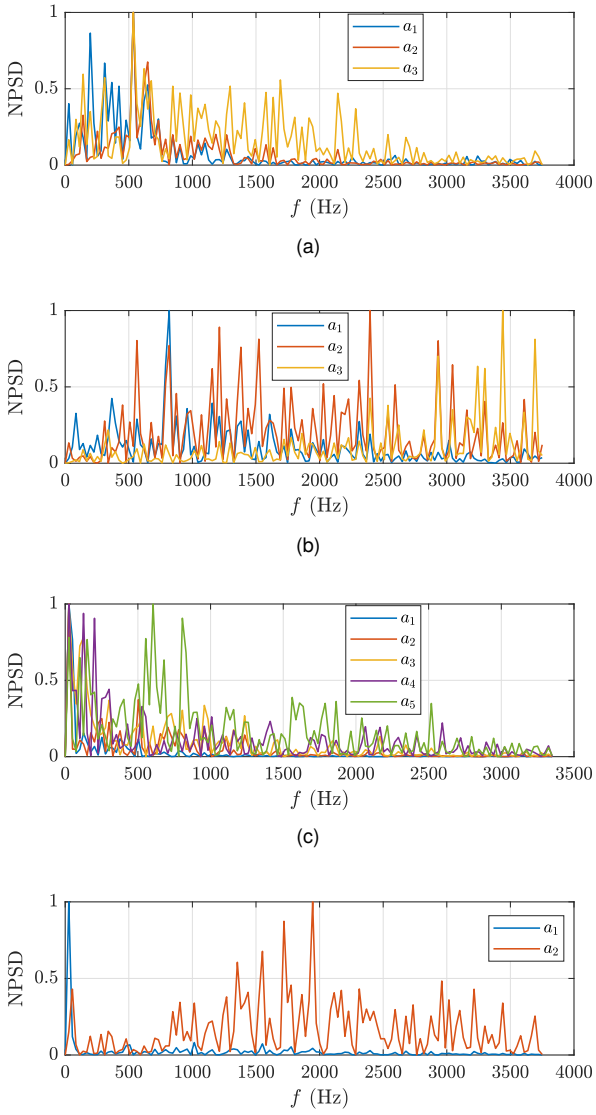

Fig. 12 NORMALISED POWER SPECTRUM DENSITY (NPSD) OF THE FIRST TWO TO FIVE POD MODES FOR: A) VISCOR, Δp = 1 BAR, p_a = 1 BAR, B) VISCOR, Δp = 3 BAR, p_a = 1 BAR, C) VISCOR, Δp = 15 BAR, p_a = 11 BAR, D) METHANOL, Δp = 15 BAR, p_a = 11 BAR.

4 Conclusions

In this paper, an attempt is made to investigate to what extent the spray dynamics of pressure-swirl atomisers used in gas turbines are affected by replacing Viscor fuel, here used as a surrogate for Diesel, with methanol. Mie-scattered spray images for different operating conditions were acquired and post-processed to resolve instantaneous axial profiles of the spray boundary. These were then averaged to determine the spray cone-angle and further post-processed with POD analysis to identify dominant wave oscillation modes embedded within the instantaneous spray boundary profiles. The following aspects were identified:

(1) Methanol showed a wider spray cone angle compared to Viscor at standard and density-adjusted pressure drop conditions.
(2) POD analysis allowed to determine dominant spatial modes, where spray boundary oscillations started to grow after an onset distance from the atomiser edge. This behaviour was consistent across all operating conditions investigated and fuels used.
(3) Lower pressure drop and ambient pressure were generally related to larger amplitude oscillations of the spray boundary and longer oscillation wavelengths. These results were consistent for both fuels and are in agreement with previous POD studies with Viscor on the same atomisers [16].
(4) Full characterisation of spray oscillation amplitudes, wavelength and oscillation onset distances for standard and density-adjusted methanol conditions indicated that Viscor and methanol are subject to similar wave dynamics for analogous operating conditions.
(5) A correlation between the SMD diameter and jet axial velocity with the oscillation amplitude of the first spatial mode was found. This was obtained for Viscor, but given the wave dynamics similarities obtained for the two fuels, could potentially be used also for methanol.

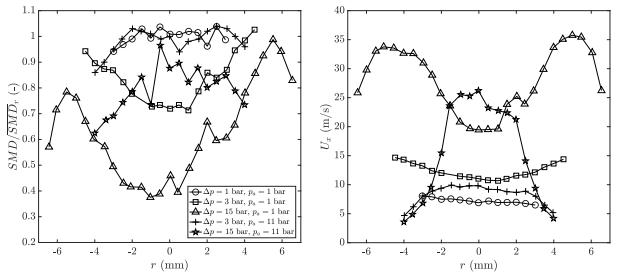

(a) (b)

Fig. 13 A) NORMALISED SMD AND B) U_x PLOTTED AGAINST RADIAL DISTANCE r FOR VISCOR [17].

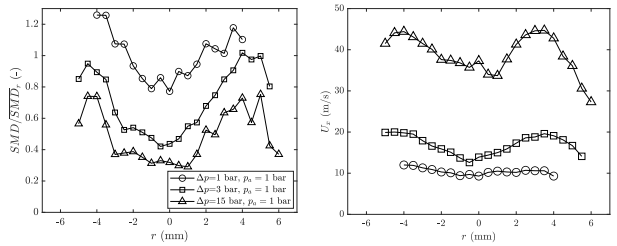

(a) (b)

Fig. 14 A) NORMALISED SMD AND B) U_x PLOTTED AGAINST RADIAL DISTANCE r FOR METHANOL.

The findings from this work will provide the foundations for understanding the relation between spray characteristics and combustion performance with different fuels, particularly when GT manufacturers are keen to operate with Methanol, HVO (Hydrogenated Vegetable Oil), Jet-A fuel for power generation and biofuels (like Biodiesel). Mie scattering based POD technique has been shown to provide strong correlations with highly accurate PDPA measurements. This offers new opportunities for the development of cost effective and unique tools towards the design and development of future gas turbine liquid injectors for various other green fuels.

Based on these considerations it can be concluded that POD can provide an effective tool to extract dominant oscillation modes of instantaneous spray dynamics, and further measurements of SMD of methanol sprays are called for to further correlate spray oscillation modes with the degree of droplet atomisation. Future research directions should extend POD analysis to axial locations further away from the nozzle (up to a distance of 32 mm which is typically monitored by GT operators) by making hardware changes to achieve increased spatial resolution and field of view, and by improving the edge detection algorithm. Moreover, POD could be applied to evaporating sprays to quantify the effects of evaporation on the spray dynamics and its modes of oscillations.

Acknowledgments

The authors gratefully acknowledge financial support from King Abdulaziz City for Technology and Science, Siemens Energy Canada Ltd and Siemens Energy Industrial Ltd (Lincoln, UK) toward this work.

Nomenclature

Symbols

p_f = Fuel supply pressure
p_{fm} = Methanol fuel supply pressure
p_{fv} = Viscor fuel supply pressure
p_a = Ambient pressure
Δp = Pressure drop
We = Aerodynamic Weber number
Re = Reynolds number
ρ_a = Ambient density
ρ_l = Liquid density
U_b = Liquid bulk velocity
d_o = Nozzle orifice diameter
σ_l = Liquid surface tension
μ_l = Liquid kinematic viscosity
θ = Spray cone angle
θ_1 = Right side spray cone angle
θ_2 = Left side spray cone angle
$\Delta\theta_{max}$ = Maximum cone angle difference
I = Surface wave oscillation
$a_i(t)$ = Temporal function of the i_{th} mode
$\mathbf{\Phi}_i(x)$ = Spatial function of the i_{th} mode
λ_i = Eigenvalue of the i_{th} mode
$A_i(x)$ = Magnitude of spray boundary oscillation
$\|a_{i-max}\|$ = Maximum absolute value of $a_i(t)$
A_{max} = Maximum amplitude
λ_{ϕ_1} = Wavelength of first POD mode
T_{ϕ_1} = Period of the first POD mode
U_x = Droplet Axial Velocity
$\overline{SMD_r}$ = Spatially averaged Sauter Mean Diameter at reference operating conditions

Acronyms

SMD = Sauter Mean Diameter
POD = Proper Orthogonal Decomposition
PDPA = Phase Doppler Particle Analyser
PSD = Power Spectral Density
NPSD = Normalised Power Spectral Density

References

[1] Guiler, R. W., 2000, "Emissions and operational aspects of methanol as an alternative fuel in a stationary gas turbine," M.S.A.E., West Virginia University, United States – West Virginia.
[2] von KleinSmid, W. H., Schreiber, H., and Klapatch, R. D., 1981, "Methanol Combustion in a 26-MW Gas Turbine," *Volume 3: Heat Transfer; Electric Power*, American Society of Mechanical Engineers, Houston, Texas, USA, p. V003T10A007.
[3] 1986, "Alternative Fuels: Potential of Methanol as a Boiler or Turbine Fuel," USGAO.
[4] Meyer, S., 2022, "One giant leap for e-Methanol," .
[5] 2023, "Methanol: a green fuel for gas turbines. SGT-A20 Bio-methanol demonstration test," Siemens Energy.
[6] Yanfeng, G., Shenghua, L., and Yu, L., 2007, "Investigation on Methanol Spray Characteristics," Energy & Fuels, **21**(5), pp. 2991–2997, Publisher: American Chemical Society.
[7] Wang, Y., Dong, P., Long, W., Tian, J., Wei, F., Wang, Q., Cui, Z., and Li, B., 2022, "Characteristics of Evaporating Spray for Direct Injection Methanol Engine: Comparison between Methanol and Diesel Spray," Processes, **10**(6), p. 1132, Number: 6 Publisher: Multidisciplinary Digital Publishing Institute.
[8] Wang, X., Gao, J., Jiang, D., Huang, Z., and Chen, W., 2005, "Spray Characteristics of High-Pressure Swirl Injector Fueled with Methanol and Ethanol," Energy & Fuels, **19**(6), pp. 2394–2401, Publisher: American Chemical Society.
[9] Badawy, T., Xu, H., and Li, Y., 2022, "Macroscopic spray characteristics of isooctane, ethanol, gasoline and methanol from a multi-hole injector under flash boiling conditions," Fuel, **307**, p. 121820.
[10] Aigal, A. K., Pundir, B. P., and Khatchian, A. S., 1986, "High Pressure Injection and Atomization Characteristics of Methanol," SAE Transactions, **95**, pp. 691–708, Publisher: SAE International.
[11] Chen, S. K., Lefebvre, A. H., and Rollbuhler, J., 1992, "Factors influencing the effective spray cone angle of pressure-swirl atomizers," ASME Journal of Engineering Gas Turbines and Power, **114**, pp. 97–103.
[12] Lumley, J. L., 1967, "The structure of inhomogeneous turbulent flows," Atmospheric Turbulence and Radio Wave Propagation, pp. 166–178.
[13] Rajamanickam, K. and Basu, S., 2017, "Insights into the dynamics of spray–swirl interactions," Journal of Fluid Mechanics, **810**, pp. 82–126.

[14] Arienti, M. and Soteriou, M. C., 2009, "Time-resolved proper orthogonal decomposition of liquid jet dynamics," Physics of Fluids, **21**(11), p. 112104.
[15] Kang, Z., Li, X., and Mao, X., 2018, "Experimental investigation on the surface wave characteristics of conical liquid film," Acta Astronautica, **149**, pp. 15–24.
[16] Ajisafe, A., Talibi, M., Ducci, A., Balachandran, R., Parsania, N., Sadasivuni, S., and Bulat, G., 2019, "Study of Dynamical Instabilities in Siemens Liquid Spray Injectors Using Complementary Modal Decomposition Techniques," American Society of Mechanical Engineers Digital Collection.
[17] Ajisafe, A. H., 2020, "Investigation of the Dynamics and Structures of Fuel Sprays in Gas Turbine Injectors," Doctoral, University College London.
[18] TSI, 2006, "Phase Doppler Particle Analyzer (PDPA)/ Laser Doppler Velocimeter (LDV): Operations Manual," .
[19] Zuiderveld, K., 1994, "Contrast Limited Adaptive Histograph Equalization," *Graphic Gems IV*, Academic Press Professional, San Diego, pp. 474–485.
[20] Otsu, N., 1979, "A Threshold Selection Method from Gray-Level Histograms," IEEE Transactions on Systems, Man, and Cybernetics, **9**(1), pp. 62–66, Conference Name: IEEE Transactions on Systems, Man, and Cybernetics.
[21] De Corso, S. M. and Kemeny, G. A., 1957, "Effect of Ambient and Fuel Pressure on Nozzle Spray Angle," Transactions of the American Society of Mechanical Engineers, **79**(3), pp. 607–614.
[22] Ortman, J. and Lefebvre, A. H., 1985, "Fuel distributions from pressure-swirl atomizers," Journal of Propulsion and Power, **1**(1), pp. 11–15.
[23] Qing-fei Fu, L.-j. Y., 2015, "Visualization studies of the spray from swirl injectors under elevated ambient pressure," Aerospace Science and Technology, **47**.
[24] Reitz, R. D. and Bracco, F. V., 1982, "Mechanism of atomization of a liquid jet," Phys. Fluids, **25**.

List of Figures

List of Tables